

# Topological edge mode morphing with reconfigurable non-Hermiticity in continuum

Honghua Qian,<sup>1,\*</sup> Jiaji Chen,<sup>1,\*</sup> Qian Wu,<sup>1,\*</sup> Shaoyun Wang,<sup>1</sup> and Guoliang Huang<sup>2,†</sup>

<sup>1</sup>*Department of Mechanical and Aerospace Engineering,  
University of Missouri, Columbia, MO 65211, USA*

<sup>2</sup>*Department of Mechanics and Engineering Science,  
College of Engineering, Peking University, Beijing 100871, PR China*  
(Dated: May 16, 2025)

Introducing non-Hermiticity into topological matter has sparked growing interest in wave physics. One particularly intriguing phenomenon is the delocalization and relocalization of non-Hermitian topological edge modes (NH-TEMs). In this work, we present the first realization of NH-TEMs in a continuum mechanical system by leveraging a one-dimensional (1D) piezoelectric-based non-Hermitian topological metabeam with sensor-actuator control. The active modulation induces non-Hermitian coupling that reshapes the conventional topological edge modes (TEMs). A full theoretical characterization of how localization evolves under varying non-Hermitian coupling strength is provided, where we reduce the Hamiltonian of the continuous media to that of a nearly metallic material, revealing the mechanism behind non-Hermitian topological morphing. Expanding this concept, we assemble a two-dimensional (2D) metaplate by stacking 1D metabeams, demonstrating reconfigurable and continuously tunable NH-TEM profiles. Experimental validations in both 1D and 2D elastic continua confirm that non-Hermiticity can be harnessed for dynamic control over energy localization and transport. These findings open a new paradigm for designing adaptive topological materials with unprecedented control over wave phenomena.

## I. INTRODUCTION

Topological matter has its roots in early studies of electronic systems, most notably the discovery of the quantum Hall effect, where the concept of topologically non-trivial phases first emerged. Today, the study of topological matter has rapidly extended beyond quantum systems into classical wave system such as optics [1–3], electromagnetism [4, 5], acoustics [6–8], and elasticity [9–11]. This applicability stems from the fact that, despite differences in their physical implementations, these systems are governed by analogous eigenvalue problems. A defining feature of such systems is the presence of topological edge modes (TEMs), which localize at the boundaries or interfaces of finite structures composed of topologically nontrivial unit cells. These edge modes are a direct manifestation of the bulk-boundary correspondence and are characterized by underlying topological invariants [12, 13]. The study of TEMs has revealed many novel phenomena and enabled diverse applications, such as robust wave propagation [14, 15], smart patterning [16], wave isolation [17], and enhanced sensing [18].

Non-Hermitian systems, which describe open quantum systems and non-conservative classical systems that exchange energy with their environment, usually exhibit complex frequency spectra [19, 20]. These systems enable a range of unconventional wave behaviors, including cloaking [21], enhanced sensitivity near exceptional point [22], odd elasticity and odd mass density [23, 24], and coherent perfect absorption and lasing [25, 26]. One

particularly intriguing phenomenon is the non-Hermitian skin effect (NHSE), in which a number of eigenstates localize at the boundaries under open boundary conditions (OBCs) [27]. These skin modes exhibit robust energy localization akin to the TEMs in Hermitian systems. However, unlike the latter, the NHSE violates the conventional bulk-boundary correspondence. Instead, it is described by a new topological invariant, the spectral winding number, which links the complex spectrum under periodic boundary conditions (PBCs) to the appearance of skin modes under OBCs [28].

Although localized modes occur in both non-Hermitian and topological systems, their origins differ fundamentally: TEMs are protected by topological invariants arising from the band structures, whereas the NHSEs emerge from nontrivial spectral windings of the complex eigenvalue spectra. The interaction between these two types of localized modes in non-Hermitian topological systems appears to be a natural and compelling research question. Recent studies have shown that non-Hermitian system can violate conventional bulk-boundary correspondence [29, 30], with a competitive mechanism observed in the non-Hermitian Su-Schrieffer-Heeger model [31, 32]. Experimental studies have further demonstrated the morphing of topological zero modes among corner, edge, and bulk states in discrete spring-mass and electrical systems [33, 34]. More recently, asymmetric delocalization of TEMs has been observed in resonance-based non-Hermitian lattices [35]. Despite these significant advances, most studies have predominantly focused on discrete lattice systems, which do not fully capture the inherent complexity and richness of continuous media. This limitation not only restricts the exploration of emergent non-Hermitian phenomena unique to continuous systems but also hampers their practical applica-

\* These authors contributed equally.

† Corresponding author:

guohuang@pku.edu.cn, huangg@missouri.edu

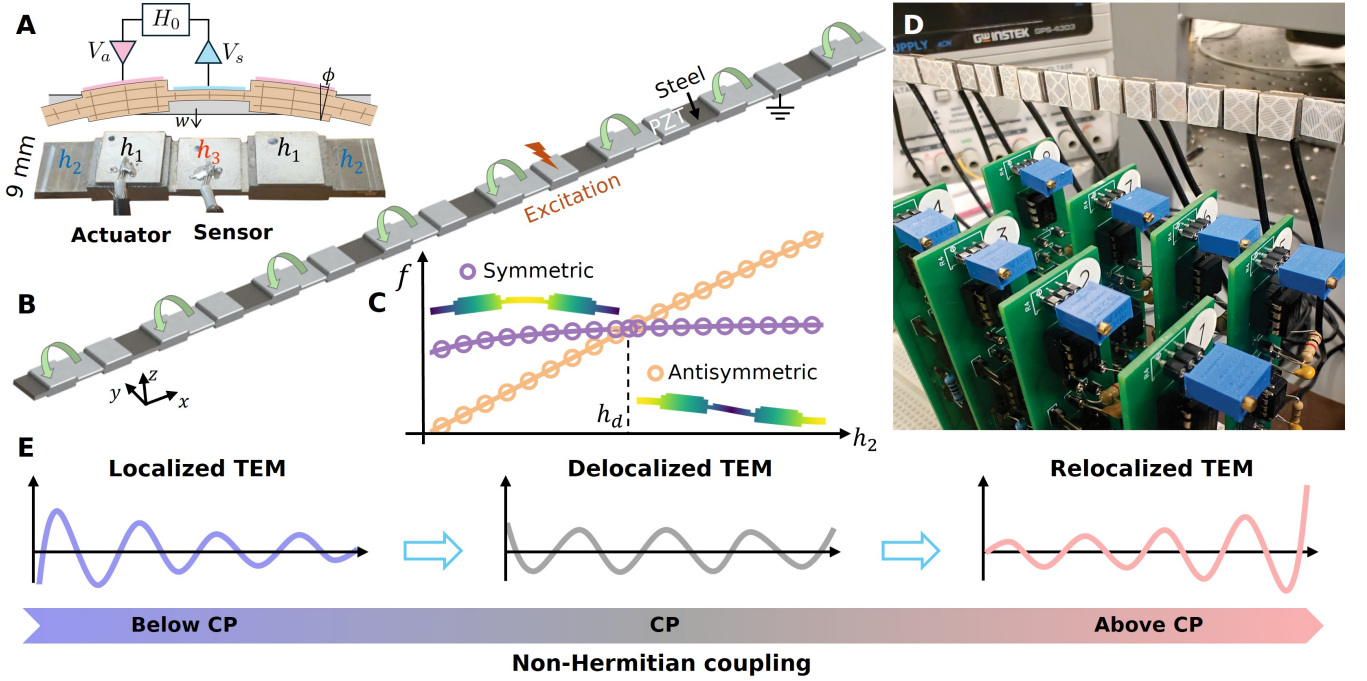


FIG. 1. Design and working principle of the non-Hermitian topological metabeam. (A) A schematic of the topological unit cell with non-Hermiticity. The continuum elastic unit cells consist of two thick cuboids connected by thin beams with different thickness, and non-Hermiticity is realized by in-cell sensing-actuating. The bending deformation  $\partial\phi_x$  is sensed by attached piezoelectric patch and outputs as a voltage signal ( $V_s$ ),  $V_s$  is amplified by coefficient  $H_0$  and then applied on the right next piezoelectric patch ( $V_a$ ), behaves an external bending moment ( $M_a$ ). (B) A segment of the piezoelectric-based non-Hermitian topological metabeam, the in-cell sensing-actuating demonstrated as the blue arrows. Thin piezoelectric patches are mounted on the steel substrate as sensors and actuators. (C) First two eigenfrequencies and corresponding eigenstates of the unit cell at the boundary of Brillouin zone. Topological phase transition can be found at  $h_2 = h_d = 0.98$  mm, where Dirac cone locates. Symmetric and antisymmetric modes exchange place at  $h_d$ , indicating the band inversion. (D) A photograph of the metabeam, the external electronic circuits in the foreground are introduced for realizing in-cell sensing-actuating. (E) Schematic representation of non-Hermitian topological morphing.

tion to real-world elastic materials and devices. To date, the experimental realization of non-Hermitian topological edge modes (NH-TEMs) in continuous elastic systems remains elusive, highlighting a critical need for an elastic platforms that can bridge theoretical predictions, computational insights, and practical implementations.

In this study, we develop an elastic platform to explore the interplay between non-Hermiticity and TEMs. The impact of non-Hermitian coupling on a thickness varied metabeam that supports TEMs is examined, where the coupling is introduced via active sensing and actuation of piezoelectric patches. To theoretically characterize the effect of non-Hermitian coupling and non-trivial topology on the NH-TEMs in the vicinity of Dirac cone, we reduce the continuum to a discrete nearly metallic analog. The resulting non-Hermitian Dirac Hamiltonian enables the precise determination of NH-TEM mode shapes. Moreover, we demonstrate that the evolution of NH-TEM can be effectively described by a non-Hermitian phase transition. Extending this concept to two dimensions, we con-

struct a non-Hermitian topological metaplate composed of metabeams stacked in parallel. The programmable non-Hermitian coupling enables diverse two-dimensional morphing of NH-TEM, as confirmed in experiment. This work lays the foundation for harnessing non-Hermitian coupling in continuous elastic topological systems, offering new strategies for adaptable and robust energy transport.

## II. RESULTS

### A. Design of a topological metabeam with reconfigurable non-Hermitian coupling

We start with the physical implementation of the topological unit cell for flexural modes. Each unit cell comprises two cuboids of thickness  $h_1$ , which are interconnected by thick beams of thickness  $h_2$  and intraconnected by thin beams of thickness  $h_3$ , as shown in Fig. 1A.

Variations in beam thickness lead to different bending stiffness, resulting in variations in intracellular and intercellular coupling strengths for flexural modes. This disparity breaks spatial inversion symmetry, giving rise to non-trivial topological properties [36]. **When intercoupling and intracoupling have the same strength, a Dirac cone can be found at the boundary of Brillouin zone ( $k_0$ )**(Fig. 1C). Our metabeam consists of eight unit cells, as shown in Fig. 1B. According to the bulk-boundary correspondence, the finite metabeam supports both a left and a right localized TEM. To investigate the effect of non-Hermitian coupling on a single TEM, we preserve the left localized TEM by removing one cuboid of the rightmost unit cell. **This approach mirrors a standard technique in topological lattice, where removing a lattice site at one end disrupts chiral symmetry of the finite structure and simultaneously changes the boundary condition** [35] (see the Supplementary Material). To introduce non-Hermitian couplings, each unit cell is equipped with piezoelectric patches that sense bending deformations and provide actuation signal. In particular, the piezoelectric patch on the interconnecting beam functions as a sensor, detecting bending curvature  $\partial\phi/\partial x$ , as shown in Fig. 1A. The output voltage is filtered and then amplified by a gain factor,  $H_0$ , which quantifies the non-Hermitian coupling strength. The amplified voltage is subsequently applied to the top surface of the piezoelectric patch on the right cuboid, which acts as an actuator, generating an external bending moment  $M_a$ . An additional piezoelectric patch is incorporated on the left cuboid to keep the mirror symmetry of the unit cell. This electrical control system enables the non-Hermitian coupling strength to be tuned with high precision.

Under Euler beam assumption, the nonlocal constitutive relation of the active beam with bending sensor-actuator reading,

$$M(x) = D_0(x)b(x) + \Delta D(x)b(x) + P\delta(x - nl_a)b(x + \delta x) \quad (1)$$

where  $D(x)$  is the bending stiffness,  $b(x) = \partial^2 w / \partial x^2$  is the bending curvature,  $P$  represents the nonlocal stiffness induced by the actuator at  $x = nl_a$ . Here we assume the sensors and actuators are all point source ??, and the actuators periodically locate at  $x = nl_a$ ,  $\delta x$  is the horizontal distance between sensor and actuator piezoelectric patches,  $b(x) = \frac{\partial^2 w}{\partial x^2}$  is the bending curvature. Under harmonic assumption of  $e^{i(kx - \omega t)}$  and the instant control, the strain-stress relations can be written as

$$M(x) = \{D(x) + P(x) [\cos(k\delta x) + i \sin(k\delta x)]\}b(x) = D_{\text{eff}}(x)b(x) \quad (2)$$

where  $D_{\text{eff}}(x)$  is a complex value represents the effective bending stiffness. Combining the equation of motion  $\frac{\partial^2 M(x)}{\partial x^2} = \rho(x)\ddot{w}$ , the general governing equation can be written as

$$\frac{\partial^2}{\partial x^2} (D_{\text{eff}}(x) \frac{\partial^2 w}{\partial x^2}) = \rho(x)\ddot{w} \quad (3)$$

Assuming that all the Bloch states at the  $k_0$  point are known, Bloch wave functions  $\psi_{n,k_0}(x) = e^{ik_0 x} u_{n,k_0}(x)$  and eigenfrequencies  $\omega_{n0}$ , where  $n$  denotes the band index, we can write the Bloch state at a wave vector  $k = k_0 + \Delta k$  near  $k_0$  as

$$\psi_{n,k}(x) = u_{n,k}(x) = \sum_j A_{n,j}(k) e^{i(k-k_0)x} \psi_{j,k_0}(x) \quad (4)$$

where the unknown periodic functions  $w_{n,k}(x)$  have been expressed as linear combinations of  $w_{j,k_0}(x)$ . Substituting Eq. 4 into Eq. 3, we obtain

$$\sum_j A_{n,j}(k) e^{i(k-k_0)x} \times \{(\omega_{n,k}^2 - \omega_{j,0}^2)\rho(x) + \mathcal{L}(x)\} \psi_{j,k_0}(x) = 0 \quad (5)$$

where  $\mathcal{L}(x)$  is a non-Hermitian operator, which details can be found in Supplementary Material. Due to matrix  $D_{\text{eff}}$  is complex, biorthogonal condition of the basis functions  $\psi_{j,k_0}(x)$  is applied  $\frac{4\pi^2}{\Omega} \int_{\text{unitcell}} \psi_{l,k_0}^L(x) \rho(x) \psi_{j,k_0}(x) dx = \delta_{lj}$ , where  $\Omega$  is the area of unit cell,  $\psi_{l,k_0}^L(x)$  is the corresponding left eigenstate of right eigenstate  $\psi_{l,k_0}(x)$ . Thus, Eq. 5 can be written as

$$\sum_j [(\omega_{j,0}^2 - \omega_{n,k}^2) \delta_{lj} + \mathcal{H}_{lj}(x)] A_{n,j}(x) = 0 \quad (6)$$

where

$$\mathcal{H}_{lj}(x) = -\frac{4\pi^2}{\Omega} \int_{\text{unitcell}} \psi_{l,k_0}^L(x) \mathcal{L}(x) \psi_{j,k_0}(x) dx \quad (7)$$

Eq. 6 has non-trivial solutions only when the following secular equation is satisfied:

$$\det [\mathcal{H} - (\omega_{n,k_0}^2 - \omega_{j,0}^2)I] = 0 \quad (8)$$

where  $\mathcal{H}$  is the effective non-Hermitian Hamiltonian. In this research, we focus on the in-gap TEM and the first gap boundary at  $k_0$ . Hence, we can only consider the first two degenerate flexural modes ( $l, j = 1, 2$ ), which greatly reduces the dimension of the continuous elastic medium to a  $2 \times 2$  non-Hermitian Hamiltonian. The two degenerate Bloch states  $\psi_{1,k_0}$  and  $\psi_{2,k_0}$  are shown in Fig. 1C, which are classified as symmetric mode and asymmetric mode via the symmetry of the deformation. The four components  $\mathcal{H}_{lj}$  in  $\mathcal{H}$  can be numerically fitted by lower boundary of band gap, gap width, corresponding frequency of TEM with OBC, approximated linear slope of the dispersion in FEM. By approximately taking the active control as the omnidirectional coupling between two degenerate states, we can further decompose the components of effective Hamiltonian as a non-Hermitian massive nearly metallic Hamiltonian as Dirac form

$$\mathcal{H} = (m - \gamma)I + (-\alpha(h_2) + \beta + \gamma) \sigma_x - i\gamma \sigma_y + \gamma \sigma_z. \quad (9)$$

$$H_{\text{eff}} = vq\sigma_z + \gamma_r I + (\beta - \gamma_r)\sigma_x - \gamma_i\sigma_y + i\gamma_i\sigma_z \quad (10)$$

where  $m$  is the massive term decides the central of the BSBG,  $\beta$  can be seen as the intercoupling,  $\alpha$  represents the intracoupling depend on the thickness  $h_2$ , and  $\gamma$  is the strength of the non-Hermitian coupling depend on the thickness  $H_0$ .

### B. Non-Hermitian phase transition of TEMs

The nontrivial TEM is predicted in a  $2N - 1$  sites OBC chain consists of the unit cell with Hamiltonian in Eq. 9, We can analytically express the top and bottom boundary of BSBG as  $\omega_t = m + (\Delta k\alpha + \beta)$  and  $\omega_b = m - (\Delta k\alpha + \beta) - \gamma$ . It can be observed that the  $\omega_b$  can be tuned by the non-Hermiticity, while the TEM frequency under OBC is immune to change with  $\gamma(H_0)$ , which can be expressed analytically as  $\omega_{\text{topo}} = m$ [37]. The unnormalized topological right eigenvector  $\Psi$  can be expressed as

$$\Psi_j = \begin{cases} (-\frac{\alpha+\lambda}{\beta})^j, & j \text{ is odd} \\ 0, & j \text{ is even} \end{cases}, \quad (11)$$

where  $j$  is the site number of finite non-Hermitian chain based on Eq. 9, and  $\frac{\alpha+\lambda}{\beta}$  is the amplified/decay ratio of TEM. It is interesting that  $\alpha(h_2)$  and  $\lambda(H_0)$  shows a competition relationship on morphing the mode profile of TEM, when  $\alpha + \lambda > \beta$ , the TEM shows an exponentially amplified TEM, while  $\alpha + \lambda < \beta$ , the TEM shows an exponentially decay TEM. Especially at  $\alpha + \lambda = \beta$ , the TEM shows an extended TEM.

$$\mathcal{W}_{\text{topo}} = \sum_{\alpha} \int_0^{2\pi} \frac{dk}{2\pi} \frac{d}{dk} \arg[\omega_{\alpha}(k) - \omega_{\text{topo}}]. \quad (12)$$

The non-Hermitian phase transition of TEM happens at the complex dispersion curve under PBC passes through the TEM frequency under OBC, corresponds to  $\omega_b - m = 0$ , which can be simplified as

$$\alpha + \lambda - \beta = 0. \quad (13)$$

It is noted that this critical non-Hermitian phase transition of TEM precisely corresponds to the extended mode profile. Similarly, the relocalized morphing of TEM happens at the  $\frac{\alpha+\lambda}{\beta} > 1$ .

The degeneracy of first two bending modes at boundary of Brillouin zone  $k = k_0 = \pi/l_a$  which happens at  $h_2 = 0.98$  mm. Figure 1E schematically shows the evolution of localization state with increasing non-Hermitian coupling strength. As the coupling strength increases from zero to a critical point (CP), the TEM transitions from a left-localized mode to a delocalized mode, which corresponds to the non-Hermitian phase transition of TEM. When the strength of non-Hermitian coupling surpasses CP, the TEM behaves as a relocalized mode with an inversed localization.

### C. Demonstration of 1D non-Hermitian morphing

To verify the ability of our designed platform to reshape the wavefunction of TEMs, we retrieve the complex frequency spectra at  $H_0 = 0, 7$  and  $10$ , as shown in Fig. 2A-C, respectively. At  $H_0 = 0$ , the metabeam is Hermitian, and the eigenfrequency of the right localized TEM falls within the bandgap between the first and second bands. In this case, the localization arise purely from the geometrical topological properties (top panel of Fig. 2D). With the non-Hermitian coupling strength taking place, the profile is reshaped, and the NH-TEM becomes an extended mode at CP  $H_0 = 7$ . Notably, the eigenfrequency of the NH-TEM remains unchanged, while the upper bound of the first band increases with increasing  $H_0$ . At the CP (Fig. 2B), the NH-TEM frequency merges with the first band, and the winding number is  $\mathcal{W} = 0$ . Further increasing  $H_0$  would change  $\mathcal{W}$  from 0 to 1, indicating the relocalization of NH-TEM to the left boundary. The mode shape of the extended and relocalized NH-TEMs in Fig. 2D confirms the results of winding phase transition. Our findings suggest that the wavefunction of our finite structure is governed by the non-Hermitian coupling strength  $H_0$ , and that actively tuning  $H_0$  provides control over the eigenmode, offering a mechanism for dynamically reshaping energy localization in non-Hermitian topological continua.

Figure 3 illustrates the phase diagram of the localization direction as a function of the non-Hermitian coefficient  $H_0$  and the reciprocal intracoupling strength  $h_2$ . When  $H_0 = 0$ , a phase transition occurs at  $h_2 \approx 0.98$  mm, where the Dirac cone is closed. Any change in  $h_2$  opens the Dirac cone, forming a bandgap and a in-gap TEM. Increasing  $h_2$  further broadens the bandgap, thereby enhancing the localization effect. In the meantime, the non-Hermitian coupling amplifies the local mode magnitude toward the right boundary, counteracting the intrinsic exponential decay of the Hermitian-TEM and morphing its profile into either an extended or left localized state. This morphing behavior is depicted in Fig. 3B, which shows the evolution of the wavefunction under varying  $H_0$ . The eigenmodes of NH-TEMs under varying  $h_2$  can be found in Fig. 3C. To efficiently determine the phase transition boundary instead of tuning the coupling strengths and observe, We calculate the critical points of non-Hermitian phase transition by effective Hamiltonian and Eq. 13, labeled gray circles in Fig. 3A.

To validate the wave morphing capability, we conduct an experiment on a metabeam in which we excite flexural waves in the middle section with piezoelectric patches. The excitation consists of a 20 cycle tone-burst signal centered at 1600 Hz. The transverse velocity fields along the metabeam are measured using a laser Doppler vibrometer as shown in Fig. 4A. Fast Fourier Transforms (FFTs) are applied to extract the normalized vibration intensity at the left and right boundaries, with results for  $H_0 = 0$  and  $10$  presented in Fig. 4B and C, respectively. In both cases, the maximum vibration intensity occurs



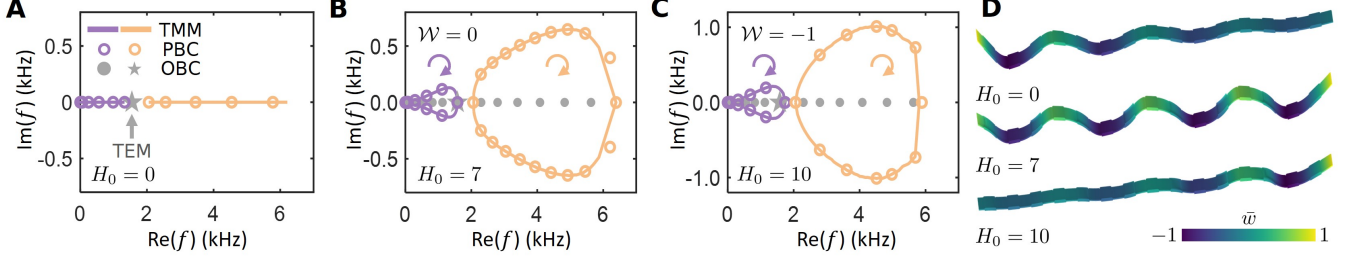


FIG. 2. Non-Hermitian phase transition in the non-Hermitian topological metabeam and corresponding topological mode. (A–C) Comparison between the PBC winding curves and the OBC frequency spectra, each corresponds to one of the three representative cases, Hermitian case, non-Hermitian winding  $\mathcal{W} = 0$ , and non-Hermitian winding  $\mathcal{W} = -1$ . The corresponding mode profiles of TEM are shown in (D–F), which behaves the localized, delocalized, and relocalized states respectively.

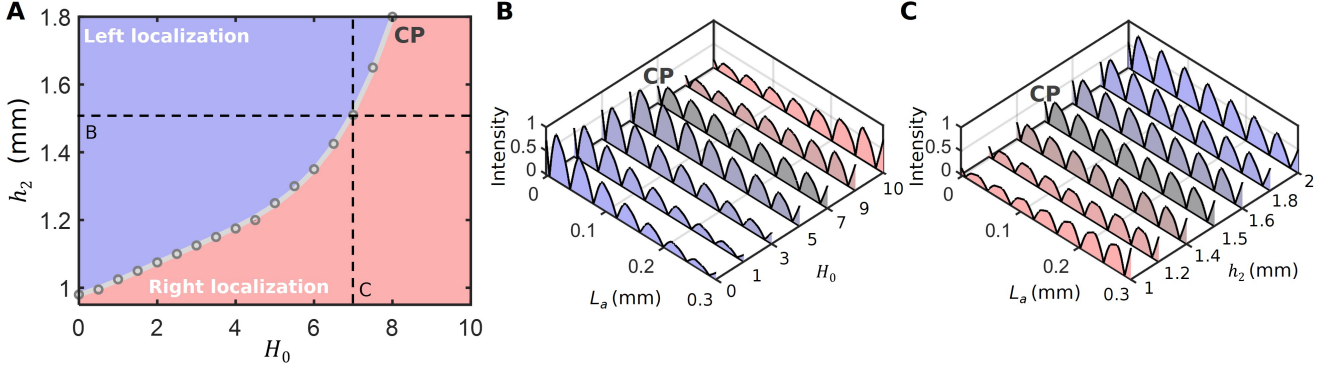


FIG. 3. Phase diagram of the localized direction of TEM, with the variation of Non-Hermitian strength( $H_0$ ) and intra-cell coupling strength( $h_2$ ). (A) Phase diagram indicating the localized direction, the prediction of critical point by TB model is marked as circles. (B) The evolution of topological mode profile with the increasing non-Hermitian strength at  $h_2 = 1.5$  mm. (C) The evolution of topological mode profile with the increasing intra-cell coupling strength at  $H_0 = 7$ .

at the NH-TEM eigenfrequency 1530 Hz. At  $H_0 = 0$ , the vibration intensity at the left boundary is significantly larger than at the right, indicating a left localized mode, and vice versa at  $H_0 = 10$ . The NH-TEM morphing behavior as a function of  $H_0$  is further illustrated in Fig. 4D–F. The experimental results confirm our prediction that the NH-TEM is left localized, extended and right localized when  $H_0 = 0, 7$  and  $10$ , respectively. These findings demonstrate that the wavefunction can be dynamically morphed into different profiles by simply tuning the non-Hermitian coupling.

#### D. Morphing of TEMs in a stacked 2D non-Hermitian topological metaplate

The experimental realization of two dimensional non-Hermitian topological morphing is demonstrated in Fig. 5. Here, we construct a 2D metaplate by stacking metabeams along the  $y$  direction, enabling morphing control in 2D space. The metaplate consists of five metabeams, each comprising six unit cells, as shown in

Fig. 5A. Neighboring metabeams are connected by thin struts, which introduce weak inter-beam coupling. This weak coupling allows energy exchange between adjacent beams without altering the TEM (see Supplementary Materials). Without loss of generality, we configure all metabeams to support a top localized TEM in the absence of non-Hermitian coupling. Similar to the 1D case, we retrieve the normalized vibration intensity from FFTs, and the mode profile of the Hermitian TEM is shown in Fig. 5B. The TEM frequency is observed at 1546 Hz, with the vibration energy localized along the top edge of the topological metaplate, gradually decaying toward the bottom edge. The corresponding FFT results for the top and bottom points in the first ( $N = 1$ ) and final ( $N = 5$ ) columns of the metaplate are shown in Figs. 5C and D, respectively.

Here, we demonstrate that the metaplate can morph into an edge-to-extended profile. The non-Hermitian coupling for each metabeam is set as  $H_N = 1.5(N - 1)$ , and the resulting NH-TEM vibration intensity profile is shown in Fig. 5E. In the first column  $H_1 = 0$ , the vibration intensity at the top point is higher than at the bot-

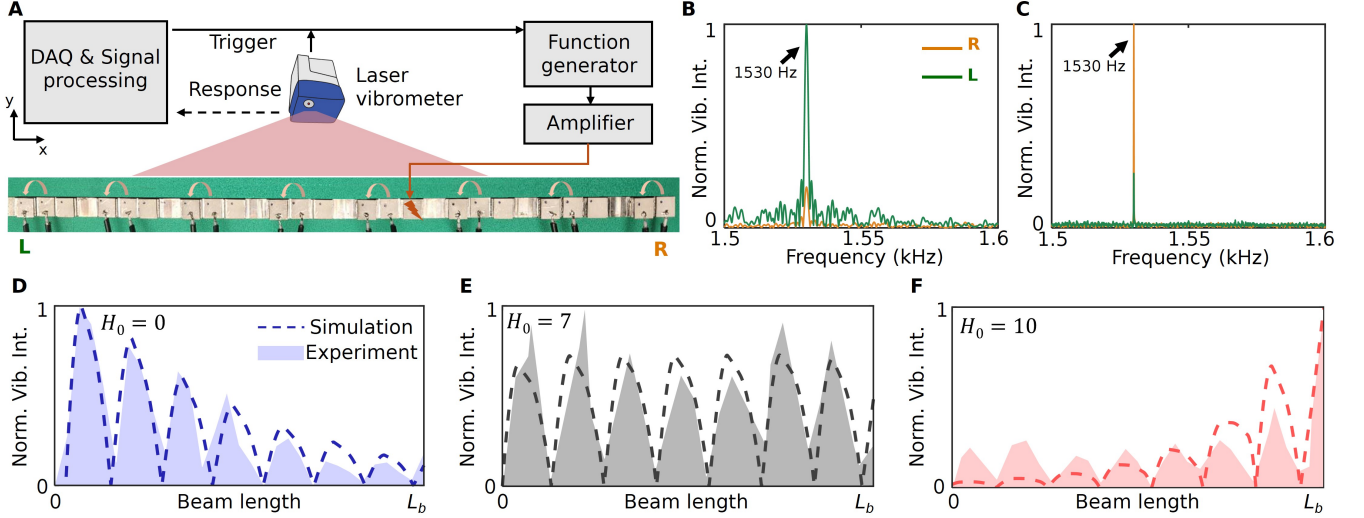


FIG. 4. Experimental demonstration of 1D non-Hermitian topological morphing. (A) Experimental setup for the demonstration of the 1D non-Hermitian topological morphing. The non-Hermitian topological metabeam is suspended on by soft strings to achieve free boundary conditions. (B) Normalized vibration intensity at both ends of the metabeam without control ( $H_0 = 0$ ). (C) Normalized vibration intensity at both ends of the metabeam with control ( $H_0 = 10$ ). (D-F) Three representative TEM shapes are demonstrated: (D) the left-localized TEM without control ( $H_0 = 0$ ); (E) the delocalized TEM resulting from the non-Hermitian phase transition at  $H_0 = 7$ ; and (F) the re-localized TEM with an inverted localization direction ( $H_0 = 10$ ).

tom, consistent with edge localization. However, in the final column ( $H_5 = 6$ ), the originally edge-localized mode transitions into an extended state. The corresponding FFT results for the top and bottom points in the first ( $N = 1$ ) and final ( $N = 5$ ) columns are shown in Figs. 5F and G, respectively. In the first column, the top point exhibits higher vibration intensity than the bottom, confirming top edge localization. Conversely, in the final column, the vibration intensities at the top and bottom points become nearly identical, indicating the transition to an extended state.

More complex NH-TEM patterns can be achieved through reconfigurable  $H_N$ , and the stacking provides an effective approach to integrating 1D metabeams into a large-scale, reconfigurable 2D metaplate to generate intricate wave patterns, as shown in Fig. 6A. In this example, ten metabeams are stacked, with  $H_N = 2\text{int}(|N - 4.5|)$  along  $y$  axis, where  $\text{int}()$  rounds a number down to the nearest integer. The leftmost metabeam ( $N = 1$ ) is Hermitian and supports a top localized TEM. As the non-Hermitian coupling strength increase linearly to 8 at the fifth metabeam ( $N=5$ ), the localization undergoes an edge-extended-edge transition. For metabeams  $N = 6$  to 10, another edge-extended-edge transition occurs in the opposite direction. These arrangements collectively form the split pattern of the non-Hermitian topological metaplate. With an excitation in the middle of bottom edge, the energy splits into two components, which can be clearly observed at the top corners of the metaplates. Furthermore, the system's topological properties ensure robustness against geometrical impurities and defects. To illustrate this, Fig. 6B depicts a non-Hermitian

defect, where four control circuits in the middle of the metaplate are removed, while Fig. 6C shows a lattice defect with a unit cell at the center of the metaplate truncated. In both cases, the resulting mode profiles still exhibit the edge-extended-edge variation of topological modes, demonstrating the system's topological robustness to multiple defects.

### III. CONCLUSION

We have experimentally and theoretically demonstrated the dynamic morphing of non-Hermitian topological edge modes in a continuous elastic system. By introducing actively tunable non-Hermiticity into a piezoelectric-based metastructure, we revealed how non-Hermitian coupling reshapes topological wave localization, enabling controlled transitions between localized, extended, and relocalized states. Our analytical framework, based on a reduced Dirac Hamiltonian, provided a fundamental understanding of these transitions, linking them to non-Hermitian phase transitions characterized by spectral winding numbers. Through experimental validation, we confirmed that tuning the non-Hermitian coupling strength in a 1D metabeam allows precise control over NH-TEM morphing. Extending this concept to 2D, we demonstrated a stacked non-Hermitian topological metaplate, where programmable non-Hermitian coupling enabled various mode morphing, including edge-extended transitions and spatial wave-splitting patterns. Additionally, we established the system's resilience against structural defects, highlight-

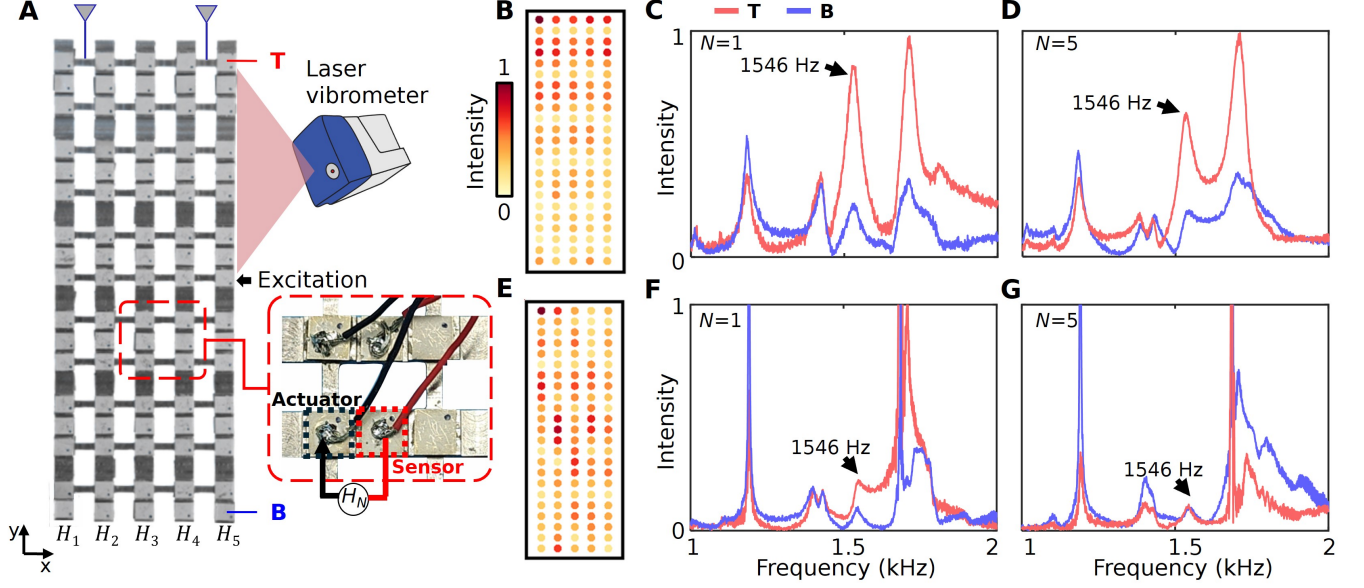


FIG. 5. Experimental configuration and results of non-Hermitian topological morphing in a 2D stacked metaplate. (A) Experimental setup for the 2D morphing experiments. The metaplate is suspended by soft strings, and the out-of-plane velocity field  $\frac{\partial w}{\partial t}$  is measured using the SLDV. A magnified view of the unit cell is shown underneath. (B) Velocity field of the passive topological metaplate ( $H_N = 0$ ). The measured frequency is 1546 Hz. (C) FFT results for the top and bottom ends of the 1<sup>st</sup> metabeam, showing higher vibration intensity at the top end than the bottom end. (D) FFT results for the top and bottom ends of the 5<sup>th</sup> metabeam. (E) Velocity field for the non-Hermitian case ( $H_N = 1.5(N - 1)$ ) from Fig. ??(C). (F) FFT results for the top and bottom ends of the 1<sup>st</sup> metabeam. (G) FFT results for the top and bottom ends of the 5<sup>th</sup> metabeam.

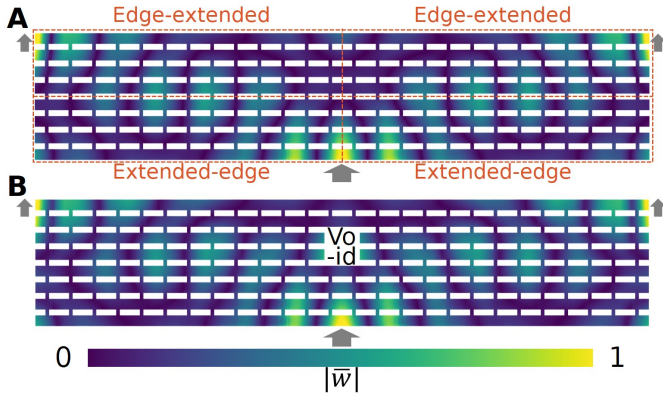


FIG. 6. Topological wave splitter by non-Hermitian morphing. (A) The normalized magnitude of  $|w|$  field distribution of the meta plate. The metaplate is integrated by 4 edge-extended patterns. (B) Robust topological wave splitter. The defect is constructed by removing 2 unit cells.

ing the robustness of non-Hermitian topological energy transport. This work marks a significant step toward harnessing non-Hermitian topology in continuous elastic media. By bridging the gap between theoretical models and practical realizations, our findings open new avenues for reconfigurable wave control, energy transport, and the design of adaptive topological materials with engineered non-Hermiticity.

## ACKNOWLEDGMENTS

This work is supported by the Air Force Office of Scientific Research under Grant No. AF 9550-18-1-0342 and AF 9550-20-1-0279 with Program Manager Dr. Byung-Lip (Les) Lee.

[1] Tomoki Ozawa, Hannah M Price, Alberto Amo, Nathan Goldman, Mohammad Hafezi, Ling Lu, Mikael C Rechtsman, David Schuster, Jonathan Simon, Oded Zilberberg, et al. Topological photonics. *Reviews of Modern Physics*, 91(1):015006, 2019.

[2] Sabyasachi Barik, Aziz Karasahin, Christopher Flower, Tao Cai, Hirokazu Miyake, Wade DeGottardi, Mohammad Hafezi, and Edo Waks. A topological quantum optics interface. *Science*, 359(6376):666–668, 2018.

- [3] Alexander B Khanikaev and Gennady Shvets. Two-dimensional topological photonics. *Nature photonics*, 11(12):763–773, 2017.
- [4] Zheng Wang, Yidong Chong, John D Joannopoulos, and Marin Soljačić. Observation of unidirectional backscattering-immune topological electromagnetic states. *Nature*, 461(7265):772–775, 2009.
- [5] Qiong Ma, Adolfo G Grushin, and Kenneth S Burch. Topology and geometry under the nonlinear electromagnetic spotlight. *Nature materials*, 20(12):1601–1614, 2021.
- [6] Haoran Xue, Yihao Yang, and Baile Zhang. Topological acoustics. *Nature Reviews Materials*, 7(12):974–990, 2022.
- [7] Cheng He, Xu Ni, Hao Ge, Xiao-Chen Sun, Yan-Bin Chen, Ming-Hui Lu, Xiao-Ping Liu, and Yan-Feng Chen. Acoustic topological insulator and robust one-way sound transport. *Nature physics*, 12(12):1124–1129, 2016.
- [8] Guancong Ma, Meng Xiao, and Che Ting Chan. Topological phases in acoustic and mechanical systems. *Nature Reviews Physics*, 1(4):281–294, 2019.
- [9] Sebastian D Huber. Topological mechanics. *Nature Physics*, 12(7):621–623, 2016.
- [10] Aoxi Wang, Yuan Zhou, and Chang Qing Chen. Topological mechanics beyond wave dynamics. *Journal of the Mechanics and Physics of Solids*, 173:105197, 2023.
- [11] D Zeb Rocklin, Shangnan Zhou, Kai Sun, and Xiaoming Mao. Transformable topological mechanical metamaterials. *Nature communications*, 8(1):14201, 2017.
- [12] J Zak. Berry’s phase for energy bands in solids. *Physical review letters*, 62(23):2747, 1989.
- [13] Weiwei Zhu, Ya-qiong Ding, Jie Ren, Yong Sun, Yunhui Li, Haitao Jiang, and Hong Chen. Zak phase and band inversion in dimerized one-dimensional locally resonant metamaterials. *Physical Review B*, 97(19):195307, 2018.
- [14] Hui Chen, Hussein Nassar, and GL Huang. A study of topological effects in 1d and 2d mechanical lattices. *Journal of the Mechanics and Physics of Solids*, 117:22–36, 2018.
- [15] Yiwei Xia, Alper Erturk, and Massimo Ruzzene. Topological edge states in quasiperiodic locally resonant metastructures. *Physical Review Applied*, 13(1):014023, 2020.
- [16] Shaoyun Wang, Zhou Hu, Qian Wu, Hui Chen, Emil Prodan, Rui Zhu, and Guoliang Huang. Smart patterning for topological pumping of elastic surface waves. *Science Advances*, 9(30):eadh4310, 2023.
- [17] Rajesh Chaunsali, Feng Li, and Jinkyu Yang. Stress wave isolation by purely mechanical topological phononic crystals. *Scientific reports*, 6(1):30662, 2016.
- [18] Kiernan E Arledge, Bruno Uchoa, Yi Zou, and Binbin Weng. Topological sensing with photonic arrays of resonant circular waveguides. *Physical Review Research*, 3(3):033106, 2021.
- [19] Yuto Ashida, Zongping Gong, and Masahito Ueda. Non-hermitian physics. *Advances in Physics*, 69(3):249–435, 2020.
- [20] Kun Ding, Chen Fang, and Guancong Ma. Non-hermitian topology and exceptional-point geometries. *Nature Reviews Physics*, 4(12):745–760, 2022.
- [21] Hao-xiang Li, María Rosendo-López, Yi-fan Zhu, Xudong Fan, Daniel Torrent, Bin Liang, Jian-chun Cheng, and Johan Christensen. Ultrathin acoustic parity-time symmetric metasurface cloak. *Research*, 2019.
- [22] Weijian Chen, Şahin Kaya Özdemir, Guangming Zhao, Jan Wiersig, and Lan Yang. Exceptional points enhance sensing in an optical microcavity. *Nature*, 548(7666):192–196, 2017.
- [23] Colin Scheibner, Anton Souslov, Debarghya Banerjee, Piotr Surowka, William TM Irvine, and Vincenzo Vitelli. Odd elasticity. *Nature Physics*, 16(4):475–480, 2020.
- [24] Qian Wu, Xianchen Xu, Honghua Qian, Shaoyun Wang, Rui Zhu, Zheng Yan, Hongbin Ma, Yangyang Chen, and Guoliang Huang. Active metamaterials for realizing odd mass density. *Proceedings of the National Academy of Sciences*, 120(21):e2209829120, 2023.
- [25] Changqing Wang, William R Sweeney, A Douglas Stone, and Lan Yang. Coherent perfect absorption at an exceptional point. *Science*, 373(6560):1261–1265, 2021.
- [26] Runcheng Cai, Yabin Jin, Yong Li, Jie Zhu, Hehua Zhu, Timon Rabczuk, and Xiaoying Zhuang. Absorption-lasing effects and exceptional points in parity-time symmetric non-hermitian metaplates. *Journal of Sound and Vibration*, 555:117710, 2023.
- [27] Xiujuan Zhang, Tian Zhang, Ming-Hui Lu, and Yan-Feng Chen. A review on non-hermitian skin effect. *Advances in Physics: X*, 7(1):2109431, 2022.
- [28] Shunyu Yao and Zhong Wang. Edge states and topological invariants of non-hermitian systems. *Physical review letters*, 121(8):086803, 2018.
- [29] Kazuki Yokomizo and Shuichi Murakami. Non-bloch band theory of non-hermitian systems. *Physical review letters*, 123(6):066404, 2019.
- [30] Shunyu Yao, Fei Song, and Zhong Wang. Non-hermitian chern bands. *Physical review letters*, 121(13):136802, 2018.
- [31] Jiwei Cheng, Xiujuan Zhang, Ming-Hui Lu, and Yan-Feng Chen. Competition between band topology and non-hermiticity. *Physical Review B*, 105(9):094103, 2022.
- [32] Weiwei Zhu, Wei Xin Teo, Linhu Li, and Jiangbin Gong. Delocalization of topological edge states. *Physical Review B*, 103(19):195414, 2021.
- [33] Wei Wang, Xulong Wang, and Guancong Ma. Non-hermitian morphing of topological modes. *Nature*, 608(7921):50–55, 2022.
- [34] Wei Lin, Banxian Ruan, Chao Liu, Xiaoyu Dai, and Yuanjiang Xiang. Evolution of topological extended state in multidimensional non-hermitian topoelectrical circuits. *Applied Physics Letters*, 125(17), 2024.
- [35] Qian Wu, Shaoyun Wang, Honghua Qian, Yanzheng Wang, and Guoliang Huang. Understanding of topological mode and skin mode morphing in 1d and 2d non-hermitian resonance-based meta-lattices. *Journal of the Mechanics and Physics of Solids*, 193:105907, 2024.
- [36] Qian Wu, Hui Chen, Xiaopeng Li, and Guoliang Huang. In-plane second-order topologically protected states in elastic kagome lattices. *Physical Review Applied*, 14(1):014084, 2020.
- [37] Jan Carl Budich and Emil J Bergholtz. Non-hermitian topological sensors. *Physical Review Letters*, 125(18):180403, 2020.
- [38] Ruben Verresen, Nick G Jones, and Frank Pollmann. Topology and edge modes in quantum critical chains. *Physical review letters*, 120(5):057001, 2018.
- [39] Roger SK Mong and Vasudha Shivamoggi. Edge states and the bulk-boundary correspondence in dirac hamiltonians. *Physical Review B*, 83(12):125109, 2011.



- [40] Ananya Ghatak, Martin Brandenbourger, Jasper Van Wezel, and Corentin Coulais. Observation of non-hermitian topology and its bulk–edge correspondence in an active mechanical metamaterial. *Proceedings of the National Academy of Sciences*, 117(47):29561–29568, 2020.
- [41] Stefano Longhi. Non-hermitian bidirectional robust transport. *Physical Review B*, 95(1):014201, 2017.
- [42] Kazuki Sone, Yuto Ashida, and Takahiro Sagawa. Exceptional non-hermitian topological edge mode and its application to active matter. *Nature communications*, 11(1):5745, 2020.
- [43] Yiwei Xia, Emanuele Riva, Matheus IN Rosa, Gabriele Cazzulani, Alper Erturk, Francesco Braghin, and Massimo Ruzzene. Experimental observation of temporal pumping in electromechanical waveguides. *Physical Review Letters*, 126(9):095501, 2021.
- [44] Weijian Zhou, Bin Wu, Zhenyu Chen, Weiqiu Chen, CW Lim, and JN Reddy. Actively controllable topological phase transition in homogeneous piezoelectric rod system. *Journal of the Mechanics and Physics of Solids*, 137:103824, 2020.
- [45] Jianfei Yin, Massimo Ruzzene, Jihong Wen, Dianlong Yu, Li Cai, and Linfeng Yue. Band transition and topological interface modes in 1d elastic phononic crystals. *Scientific reports*, 8(1):6806, 2018.
- [46] Qian Wu, Xiaodong Zhang, P Shivashankar, Yangyang Chen, and Guoliang Huang. Independent flexural wave frequency conversion by a linear active metalayer. *Physical Review Letters*, 128(24):244301, 2022.
- [47] Yangyang Chen, Xiaopeng Li, Colin Scheibner, Vincenzo Vitelli, and Guoliang Huang. Realization of active metamaterials with odd micropolar elasticity. *Nature communications*, 12(1):5935, 2021.
- [48] Meng Xiao, Guancong Ma, Zhiyu Yang, Ping Sheng, ZQ Zhang, and Che Ting Chan. Geometric phase and band inversion in periodic acoustic systems. *Nature Physics*, 11(3):240–244, 2015.
- [49] Nesbitt W Hagood and Andreas Von Flotow. Damping of structural vibrations with piezoelectric materials and passive electrical networks. *Journal of sound and vibration*, 146(2):243–268, 1991.
- [50] Zhenguo Zhang, Feng Chen, Zhiyi Zhang, and Hongxing Hua. Vibration analysis of non-uniform timoshenko beams coupled with flexible attachments and multiple discontinuities. *International Journal of Mechanical Sciences*, 80:131–143, 2014.
- [51] Qian Wu, Honghua Qian, Yangyang Chen, and Guoliang Huang. Dynamic phononic crystals with spatially and temporally modulated circuit networks. *Acta Mechanica Sinica*, 39(7):723007, 2023.
- [52] Yisheng Zheng, Junxian Zhang, Yegao Qu, and Guang Meng. Adaptive nonreciprocal wave attenuation in linear piezoelectric metastructures shunted with one-way electrical transmission lines. *Journal of Sound and Vibration*, 503:116113, 2021.
- [53] M Zahid Hasan and Charles L Kane. Colloquium: topological insulators. *Reviews of modern physics*, 82(4):3045–3067, 2010.
- [54] Xiao-Liang Qi and Shou-Cheng Zhang. Topological insulators and superconductors. *Reviews of modern physics*, 83(4):1057–1110, 2011.
- [55] Farzad Zangeneh-Nejad, Andrea Alù, and Romain Fleury. Topological wave insulators: a review. *Comptes Rendus. Physique*, 21(4-5):467–499, 2020.
- [56] János K Asbóth, László Oroszlány, and András Pályi. A short course on topological insulators. *Lecture notes in physics*, 919(1), 2016.
- [57] Singiresu S Rao. *Vibration of continuous systems*. John Wiley & Sons, 2019.